Gate-Tunable Strong Spin–Orbit Torque in 2D Weyl Semiconductor Tellurium-Based Heterostructures

Qiqi Zhang(张琦琦)[1†], Xiaoyu Xiong(熊小语)[2,3†], Hongjun Xu(许洪军)[4], Congli He(何聪丽)[2,3*], Chaoqun Hu(胡超群)[2,3], Hao Yu(于昊)[6], Chunli Zhao(赵春丽)[2], Jiayi Chen(陈佳怡)[2,3], Haochang Lyu(吕浩昌)[1], Ruifen Dou(窦瑞芬)[2], Shipeng Shen(申世鹏)[2,3], Guoqiang Yu(于国强)[5], Jinxing Zhang(张金星)[2,3], and Shouguo Wang(王守国)[2,6*]

[1]*Beijing Superstring Academy of Memory Technology, Beijing 100176, China*
[2]*School of Physics and Astronomy, Beijing Normal University, Beijing 100875, China*
[3]*Key Laboratory of Multiscale Spin Physics (Ministry of Education), Beijing Normal University, Beijing 100875, China*
[4]*Key Laboratory for Magnetism and Magnetic Materials of the Ministry of Education, Lanzhou University, Lanzhou 730000, China*
[5]*Beijing National Laboratory for Condensed Matter Physics, Institute of Physics, Chinese Academy of Sciences, Beijing 100190, China*
[6]*Anhui Provincial Key Laboratory of Magnetic Functional Materials and Devices, School of Materials Science and Engineering, Anhui University, Hefei 230601, China*

(Received 8 January 2026; accepted manuscript online 12 March 2026)

Two-dimensional (2D) Te possesses a unique chiral crystal structure and strong spin–orbit coupling, making it a promising material platform for the study of spin–orbit torque (SOT). In this work, we systematically investigate the gate-tunable electrical transport and SOT efficiency in high-quality 2D Te synthesized via a hydrothermal method. Electrical transport measurements reveal a pronounced gate-tunable negative magnetoresistance (NMR), indicating strong spin–orbit interactions and a characteristic topological band structure in the Te flakes. We further demonstrate that the SOT efficiency in Te/Py heterostructures is comparable to that of conventional heavy metals. Importantly, the SOT efficiency can be effectively modulated by a back-gate voltage, achieving a tunability of up to 15%. This study not only confirms 2D Te as an efficient SOT material, but also offers new pathways toward developing low-power, electrically tunable spintronic devices.

DOI: 10.1088/0256-307X/43/4/040712 CSTR: 32039.14.0256-307X.43.4.040712

1. Introduction. Spin–orbit torque (SOT) effect is one of the core physical effects for developing next-generation spin-based logic devices[1,2] and memory chips.[3,4] It enables efficient and rapid manipulation of magnetic moments by harnessing spin currents originating from strong bulk or interfacial spin–orbit coupling (SOC).[5,6] Early research on SOC materials has primarily focused on heavy metals such as Pt,[7] W,[8] and Ta.[9] In recent years, topological materials (including topological insulators[10,11] and magnets[12,13]) along with two-dimensional (2D) materials have also received increasing attention. Notably, 2D materials have emerged as promising candidates for spintronic devices due to their diverse crystal structures and symmetries, tunable electronic structures, and van der Waals interfaces. Many non-magnetic 2D materials (such as MoS_2,[14,15] WSe_2,[14] WTe_2,[16,17] $TaIrTe_4$,[18,19] and $PtTe_2$[17,20]) have been successfully employed to generate SOTs, demonstrating rich physical properties and a broad range of electronic tunability. Simultaneously, magnetic 2D materials (such as Fe_3GeTe_2[21,22] and $Cr_2Ge_2Te_6$[23]) have also been successfully integrated into SOT architectures, demonstrating comparable functional versatility. By combining both SOC-active and magnetic 2D components, integrated 2D SOT heterostructures hold significant promise as core elements in future spintronic technology.

Among various non-magnetic 2D materials, 2D tellurium[24] has attracted great research interest due to its remarkable physical characteristics, such as high carrier mobility, tunable bandgap, strong light–matter interaction, excellent environmental stability, and pronounced structural anisotropy.[25–29] More importantly, Te is recognized as a novel Weyl semiconductor with symmetry-protected Weyl nodes near the band edges.[30] Such a topological property stems from its unique helical chain structure, inherently breaking the spatial inversion symmetry. Combined with the strong SOC of heavy Te atoms, 2D Te is not only promising for generating large SOTs but may also be useful for generating unconventional SOT components.[31] Meanwhile, recent studies have demonstrated various electric-field-tunable modulation

†These authors contributed equally to this work.
*Corresponding authors. Email: conglihe@bnu.edu.cn; sgwang@ahu.edu.cn
© 2026 Chinese Physical Society and IOP Publishing Ltd. All rights, including for text and data mining, AI training, and similar technologies, are reserved.

mechanisms in SOT devices, such as utilizing ferroelectric/multiferroic control,[32,33] ion migration,[34,35] and electrostatic doping.[36,37] The Fermi level of Te can be effectively tuned by a gate voltage,[28] offering a platform to investigate the correlation between electronic band structure and SOT in Te-based devices. However, the SOT effect in Te and its gate tunability remain unexplored.

In this paper, high-quality Te flakes were synthesized via the hydrothermal method, and their magnetoelectric transport properties and gate-tunable SOT effects were investigated. Firstly, we characterized the structural properties of the Te flakes, and then studied the chirality-dependent magnetotransport, which revealed the negative magnetoresistance (NMR) associated with the chiral anomaly current. To study the gate-tunable SOT efficiency, two types of Te-based magnetic heterojunctions were fabricated (Te/Py and Te/MgO/Py), measured by spin-torque ferromagnetic resonance (ST-FMR). We demonstrated a notable SOT efficiency in the Te/Py magnetic heterojunctions, which is comparable to that of conventional heavy metals. By inserting an ultrathin MgO layer to weaken the Fermi pinning at the Te/Py interface, a 15% modulation of SOT efficiency in Te/MgO/Py heterojunction has been achieved by applying a back-gate voltage. These findings offer crucial insight into the preparation of Te-based magnetic heterojunctions and their applications in voltage-tunable spintronic devices.

2. Experimental Section.

2.1. Synthesis of Te Flakes. The large-area Te flakes were prepared via hydrothermal synthesis [Supplementary Materials (SM), Fig. S1]. Firstly, 120 mg of Na_2TeO_3 and 1 g of polyvinylpyrrolidone were fully dissolved in 30 mL of deionized (DI) water to form a mixed solution. Then, 1.5 mL of hydrazine monohydrate and 3 mL of ammonium hydroxide solution were added to the mixture. The solution was transferred into a 50 mL Teflon-lined stainless steel autoclave, gradually heated to 180 ℃, and maintained for 40 hours. Subsequently, the synthesized product was cleaned with DI water by centrifuging several times at 5000 rpm. Finally, the product was dispersed in DI water for further use. The purified Te suspension was deposited onto p-type, heavily doped Si substrates capped with a 300 nm-thick SiO_2 layer to fabricate Te nanoflake devices and Te-based heterojunctions.

2.2. Characterization of Te Flakes. The surface morphology and thickness were measured by atomic force microscopy (AFM) using a Multimode 8 AFM (Bruker) in tapping mode. Raman spectra were acquired on a LabRAM HR Evolution Raman system (Horiba) with an excitation wavelength of 532 nm. The crystal structures were analyzed via a D8 ADVANCE X-ray diffractometer (XRD) (Bruker) equipped with a Cu $K\alpha$ radiation source ($\lambda = 1.541$ Å). Chemical compositions were determined by an ESCALAB 250Xi X-ray photoelectron spectrometer (XPS) (Thermo Fisher Scientific). Transmission electron microscopy (TEM) images, high-resolution TEM (HRTEM), high-angle annular dark-field scanning transmission electron microscopy (HAADF-STEM), and energy-dispersive X-ray spectroscopy (EDS) mapping were analyzed by a JEM-ARM200F TEM (JEOL, Tokyo, Japan) equipped with double Cs correctors, using cross-sections prepared by a focused ion beam system.

2.3. Fabrication of Te-Based Magnetic Heterojunction Devices. To investigate the magnetoelectric transport characteristics of Te, Te and Te-based magnetic heterojunctions were processed into devices. The Te flakes were patterned into Hall bar structures via ultraviolet (UV) lithography, followed by the deposition of Pt (10 nm)/Au (100 nm) electrodes using a lift-off process. To fabricate Te-based magnetic heterojunction devices, Py (6 nm)/MgO (2 nm)/W (2 nm) or MgO (0.6 nm)/Py (6 nm)/MgO (2 nm)/W (2 nm) were successively deposited onto the Te flakes via high-vacuum magnetron sputtering. The MgO/W bilayer serves a dual purpose as a capping layer. The top 2-nm W layer protects against oxidation, and the bottom 2-nm MgO layer blocks the spin current[38] from the underlying W. The 0.6-nm MgO[39] between Te and Py layers serves to mitigate the Fermi pinning. After deposition, the samples were patterned into rectangular microstrips using UV lithography combined with Ar ion milling, and then the contact Pt (10 nm)/Au (100 nm) electrodes were made via a lift-off process for ST-FMR measurements.

2.4. Magneto-Transport Measurements and ST-FMR Measurements. Magneto-transport measurements were performed in a physical property measurement system (PPMS, Quantum Design). A Keithley 2400 was used to apply the back-gate voltage and measure the corresponding leakage current, while a 6221 current source (Keithley) and a 2182A nanovoltmeter (Keithley) measured the resistance in the channel. For ST-FMR measurement, an SMB100A signal generator (Rohde & Schwarz) generated radio frequency current (I_{RF}), and the rectified DC voltage was detected by an SR830 Lock-In Amplifier (Stanford Research Systems).

3. Results and Discussion.

3.1. Structural Characterization of Single-Crystal Tellurium. The crystal structure of Te comprises distinctive chiral helical chains extending along the *c*-axis. Within each chain, atoms are covalently bonded, and adjacent parallel chains are interconnected via van der Waals interactions, as shown in Fig. 1(a). The optical microscope image in Fig. 1(b) shows that Te flakes are randomly dispersed on the substrate, exhibiting irregular shapes and sizes of approximately 10–200 μm. The thickness of the sample, as determined by AFM [as shown in Fig. 1(c)], is around 32 nm. The inset presents the surface topographic image with an average roughness of about 0.16 nm. XRD and XPS were employed to characterize the crystal structure and chemical compositions of Te flakes, respectively (SM, Fig. S2). The XRD pattern [SM, Fig. S2(a)] reveals diffraction peaks corresponding to the (100), (101), (110), and (200) planes, confirming the high crystallinity of the sample. In the XPS spectrum [SM, Fig. S2(b)], in addition to the intrinsic signals from elemental Te, peaks of Te^{4+} were observed, indicating inevitable surface oxidation.

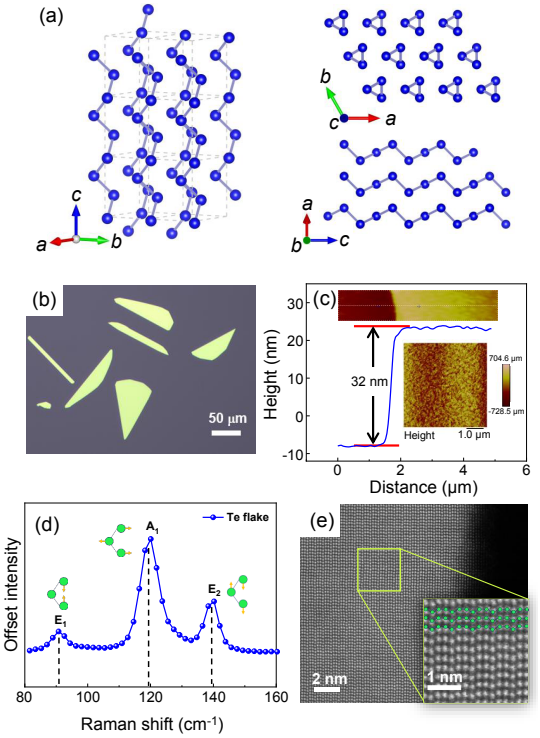

Fig. 1. (a) The schematic diagram for Te crystal structure viewed along the a- and c-axes directions. (b) Optical image of the Te flakes; the scale bar is 50 μm. (c) AFM image of the 2D flake, showing a thickness of around 32 nm. The insets display the corresponding scan path and surface roughness image. (d) Raman spectra of the Te flake; the inset shows the atomic vibration directions of the E_1, A_1, and E_2 optical modes. (e) HAADF-STEM images of Te flake viewed along the a-axis; the inset shows a magnified view. The scale bars are 2 nm and 1 nm, respectively.

To further verify the crystal quality at the microscopic level, both Raman and TEM characterizations were performed on the Te flakes. As shown in Fig. 1(d), the Raman spectrum exhibits three characteristic peaks, identified as the A_1 mode (120.1 cm^{-1}), E_1 mode (90.7 cm^{-1}), and E_2 mode (140.2 cm^{-1}), which correspond to the chain expansion mode arising from atomic motion within the basal plane, the bond bending mode involving rotation in the basal plane, and the asymmetric bond stretching mode along the c-axis, respectively.[25] Figure 1(e) presents a HAADF-STEM image of the Te flake viewed along the a-axis, confirming a well-defined crystal structure. Collectively, these structural characterizations demonstrate the high crystallinity and quality of the synthesized Te flakes.

3.2. Magneto-Transport Properties of Tellurium Flakes. The electrical properties and gate-controlled NMR of Te flakes were measured at various temperatures. The Te flakes were uniformly dispersed on the p-doped Si substrate and patterned into the standard Hall-bar structure for transport measurement. The long edge of the Te flakes aligns with the crystallographic c-axis, as shown in Fig. 2(a). With the current applied to the device along the c-axis, the longitudinal resistance R_{xx} gradually increased as the back-gate voltage V_G swept from −30 V to 30 V, indicating a typical p-type conduction behavior [see Fig. 2(b)]. Figure 2(c) presents the Hall resistance R_{xy} as a function of the perpendicular magnetic field at various V_G. The Hall mobility μ of the Te flake sample can be calculated by the following formula:[26]

$$\mu = \frac{R_{xy}}{R_{xx}} \frac{1}{B} \frac{L}{W}, \tag{1}$$

where B is the magnetic field, L and W denote the length and width of the Te channel, respectively. The calculated Hall mobility values at various V_G are summarized in Table 1. The Hall mobility degradation under both negative and positive back-gate bias is attributed to distinct mechanisms. Under negative bias, gate-induced carrier redistribution towards the interface, enhances scattering effects from interface roughness.[26] And under positive bias, the reduced carrier density weakens the screening effect against charged impurities.[28]

Table 1. Hall mobility of Te flakes under various back-gate voltages.

V_G (V)	μ ($cm^2 \cdot V^{-1} \cdot S^{-1}$)
30	129.25
0	379.82
−30	218.14

In the Weyl semimetal Te, under external in-plane magnetic and electric fields, the chiral symmetry of the Weyl nodes is disrupted, inducing a chiral current in the Weyl material. The NMR usually serves as one of the characteristic transport behaviors of the chiral anomaly,[40] thus indicating the topological state of the system. Consequently, the characteristic evolution of the Te band structure can be effectively probed via back-gate voltage modulation. The magnetoresistance (MR) of the sample is defined as: $\text{MR} = (R_B/R_0 - 1) \times 100\%$, where R_0 and R_B are the resistances at zero magnetic field and under a perpendicular magnetic field B, respectively. As shown in Fig. 2(d) ($V_G = 0$ V), the NMR behavior is clearly observed in Te flakes, demonstrating the typical Weyl physics in Te. To better study the relationship between the Fermi level and chiral transport behavior, the Fermi level of the Te flake was precisely tuned by applying a back-gate voltage. When the back-gate voltage was varied from −20 V to 20 V, the measured NMR value first increased and then decreased to the normal MR. The NMR peak occurs at $V_G \approx -7$ V, with the corresponding value about 1.75 times larger than that at $V_G \approx 1$ V, as shown in Fig. 2(e). The significant enhancement of the NMR signal indicates that the Fermi level has shifted closer to the Weyl nodes in Te,[41] which is attributed to the intensified Berry curvature distribution arising from proximity to the Weyl nodes. Meanwhile, the NMR magnitude can be effectively tuned by applying a back-gate voltage to modulate the relative position between the Fermi level and the Weyl nodes. Figure 2(f) shows the MR modulation of the Te flakes by the back-gate voltage under a perpendicular magnetic field. A comparison of MR between parallel magnetic field (for NMR) and perpendicular magnetic field (for weak localization) under identical V_G is summarized in Fig. S3 of the

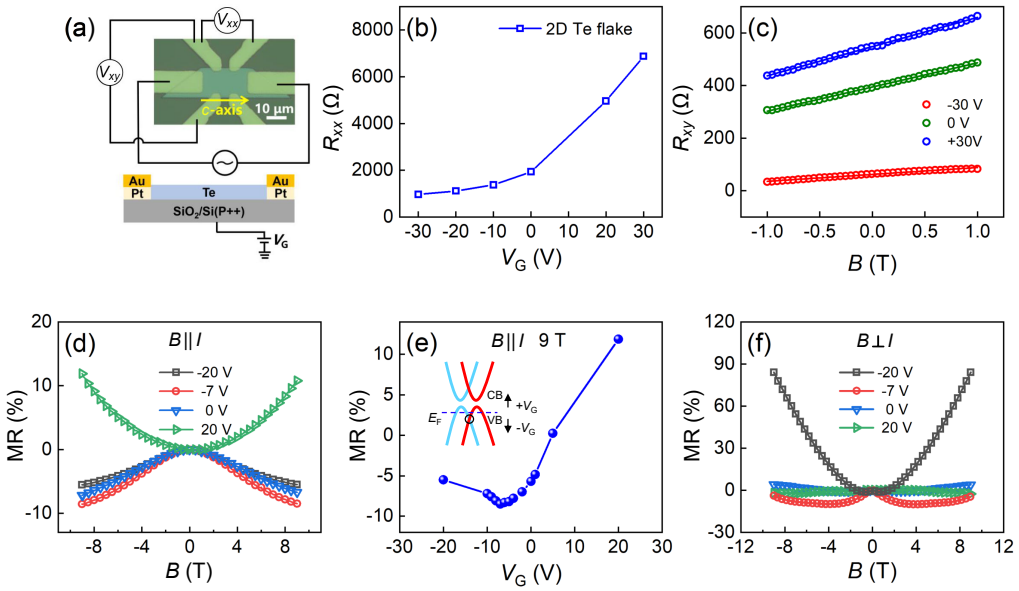

Fig. 2. The magneto-transport properties of Te flakes. (a) Schematic diagram of the electronic transport measurement device structure; the scale bar is 10 μm. (b) The longitudinal resistance (R_{xx}) of Te as a function of back-gate voltage (V_G) with a thickness of 20 nm. (c) Hall resistance (R_{xy}) as a function of perpendicular magnetic field ($B \perp I$), at various back-gate voltages $V_G = -30$, 0, and 30 V. (d) The MR as a function of magnetic field at different V_G for the Te flake device with a thickness of 39 nm at a temperature of $T = 2$ K, with $B \parallel I$. (e) MR as a function of V_G at $B = 9$ T and $T = 2$ K, demonstrating gate-tunable MR. The inset illustrates the regulation of the Fermi level by the back-gate voltage. (f) MR as a function of magnetic field at different V_G, with $B \perp I$.

SM. Notably, the strength of the weak localization behavior changes from strong to weak upon decreasing the negative back-gate voltage from −20 V to −7 V, reflecting weak SOC near the Weyl nodes.[28,42]

3.3. Spin–Orbit Torque in Te-Based Magnetic Heterostructures. The Te/Py heterostructure was prepared to investigate the SOT efficiency of the Te layer, which is characterized by ST-FMR measurements. The measurement configuration is illustrated in Fig. 3(a), where I_{RF} denotes the microwave current applied to the device and J_S indicates the direction of the spin current. I_{RF} was injected along three crystallographic directions: the *c*-axis [inset of Fig. 3(b)], at a 45° angle from the *c*-axis [inset of Fig. 3(c)], and the *a*-axis [inset of Fig. 3(d)], respectively. The measurements are conducted at a fixed in-plane angle $\varphi = 40°$ between the current and the external magnetic field H_{ext}. Figures 3(b)–3(d) display the frequency-dependent rectified mixing voltage spectra V_{mix} over the range of 6 GHz to 12 GHz. The V_{mix} spectra can be fitted by the Lorentzian function,[7]

$$V_{mix} = V_S \frac{\Delta H^2}{(H_{ext} - H_r)^2 + \Delta H^2} + V_A \frac{\Delta H (H_{ext} - H_r)}{(H_{ext} - H_r)^2 + \Delta H^2} + V_0, \quad (2)$$

where V_S and V_A are the symmetric and antisymmetric Lorentzian coefficients, ΔH is the linewidth, H_r is the resonance field, and V_0 is a constant offset. The resonance frequency f versus H_r follows the Kittel formula,[43]

$$f = \left(\frac{\gamma}{2\pi}\right)\sqrt{H_r(H_r + 4\pi M_{eff})}, \quad (3)$$

where γ is the gyromagnetic ratio of Py, and $4\pi M_{eff}$ is the effective magnetization. Furthermore, the angular dependence of V_S and V_A, acquired by varying the angle φ between I_{RF} and H_{ext}, as shown in Figs. 3(e)–3(g), which can be well fitted by $\cos\varphi \sin 2\varphi$, reveals that no unconventional SOT is observed in the system. The SOT efficiency ξ_{SOT} can be quantitatively evaluated using the following equation:[7]

$$\xi_{SOT} = \frac{V_S e}{V_A \hbar} \mu_0 M_S d_{NM} d_{FM} \sqrt{1 + \frac{4\pi M_{eff}}{\mu_0 H_r}}, \quad (4)$$

where e is the electron charge, $\hbar$ is the reduced Planck constant, μ_0 is the vacuum permeability, M_S is the saturation magnetization of the Py layer, and d_{NM} and d_{FM} are the thicknesses of the Te and Py layers, respectively. The SOT efficiency is determined to be approximately 0.12, which is comparable to that of heavy metals such as Pt.[7,44] While recent reports indicate a small field-like torque in Te-based systems,[20] the calculated SOT efficiency is dominated by the damping-like torque. The field-like contributions included in this value can be further disentangled via Py thickness-dependent measurements.[45,46] Furthermore, recent theoretical[47] and experimental[48] studies have found that electric current induces orbital and spin magnetization in helical-crystal Te, which can exert a torque on the ferromagnet. The Ni-rich ferromagnetic Py layer probably acts as an efficient converter of orbital angular momentum to spin angular momentum; thus, the SOT within the system may arise from the combined effects of spin- and orbital-related contributions in the Te layer. However, as V_G is tuned from −20 V to +10 V, there is no significant change in the ST-FMR spectra, and

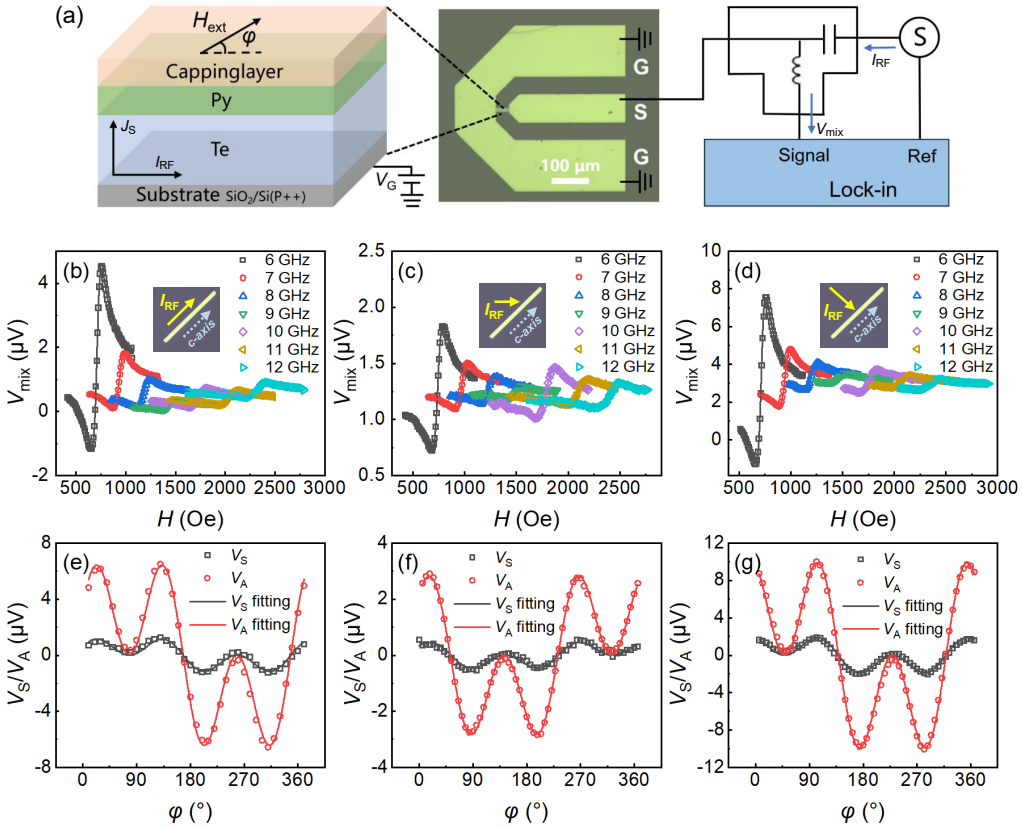

Fig. 3. ST-FMR measurement of the Te (15 nm)/Py (6 nm) heterostructure. (a) Schematic of the ST-FMR measurement setup; the scale bar is 100 μm. (b)–(d) Frequency-dependent ST-FMR spectra (V_{mix}), measured at frequencies of 6–12 GHz with the power of 13 dBm. The RF current I_{RF} is applied along (b) the c-axis, (c) 45° from the c-axis, and (d) 90° from the c-axis (along the a-axis), as illustrated in the insets. The symbols and solid curves represent the experimental data and the fitting results, respectively. (e)–(g) Angular dependence of the symmetric (V_S) and antisymmetric (V_A) components of V_{mix} for I_{RF} along (e) the c-axis, (f) 45° from the c-axis, and (g) 90° from the c-axis (along the a-axis), respectively.

the SOT efficiency remains nearly constant under various V_G (see SM, Fig. S4). This gate-independent behavior may be related to the Fermi-level pinning effect, caused by a high density of metal-induced gap states at the Te/Py interface.[49] TEM technology is used to characterize the Te/Py interface, as shown in Figs. S5(a) and S5(c) of the SM. The HRTEM image, HAADF-STEM image, and the corresponding EDS mappings of Te, Fe, Ni, O, and Mg in the Te/Py structure show that Ni atoms from the Py layer diffused into the crystal lattice of the Te flake, forming a Ni-doped region at the interface of the Te layer adjacent to the Py layer with a thickness of approximately 5–10 nm. This may explain the absence of unconventional SOT as well as the gate-tunable SOT in the system.

3.4. Gate-Tunable Spin–Orbit Torque in Te/MgO/Py Magnetic Heterostructures. To mitigate Fermi-level pinning at the metal–semiconductor interface, various strategies have been explored, including inserting ultrathin insulating interlayers,[50] employing van der Waals contacts,[51] and heavily doping the contact region.[52] In this work, an ultrathin MgO layer (∼0.6 nm) was inserted between the Te and Py layers to prevent direct contact, as shown in Fig. 4(a). The TEM and EDS characterizations indicate that the MgO layer effectively mitigates Ni diffusion into Te, showing an obvious reduction compared to the direct-contact structure [see SM, Figs. S5(b) and S5(d)]. The SOT efficiency of the Te/MgO/Py magnetic heterostructure is further characterized by ST-FMR measurements. The calculated SOT efficiency is approximately 0.089 at $V_G = 0$ V [as shown in Fig. 4(b)], which is lower than that of the Te/Py structure; this reduction can be attributed to the MgO interlayer decreasing the spin transparency.[38] However, notably, the SOT efficiency in the Te/MgO/Py heterostructure can be modulated by applying a back-gate voltage. As V_G varied from −10 V to +10 V, clear variations in the rectification signal were observed in Fig. 4(c), indicating that the introduction of the MgO layer effectively suppresses the Fermi-level pinning effect. The SOT efficiency under different back-gate voltages is quantified by Eq. (4), which demonstrates a gate-tuning range of up to 15% [see Fig. 4(d)]. ST-FMR measurements of the Te/MgO/Py heterostructure before and after back-gate voltage application are provided in Fig. S6 of the SM, indicating that the device remains intact and restored to its original state after gate application.

Previous studies have found that the SOT efficiency can be effectively modulated in various systems, such as magnetically doped topological insulators $[Cr_{0.16}(Bi_{0.50}Sb_{0.42})_2Te_3]$,[36] 2D semiconductor systems (WS_2),[37] and magneto-ionic systems (e.g., Pt/Co/GdO_x heterostructures),[34] exhibiting SOT enhancement or sign reversal. In contrast to other architectures that are often

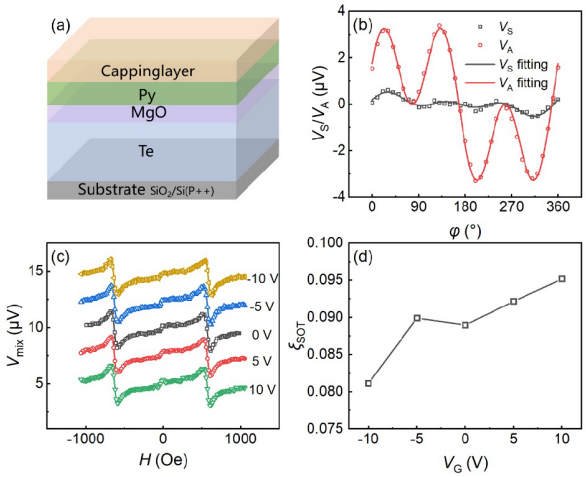

Fig. 4. Gate-tunable SOT in a Te (15 nm)/MgO (0.6 nm)/Py (6 nm) heterostructure. (a) Schematic of the Te/MgO/Py device structure. (b) The field-angle dependence of V_S and V_A for the Te/MgO/Py; the symbols and curves represent the experimental data and the fitting results, respectively. (c) The ST-FMR spectra measured at various back-gate voltages from −10 V to 10 V. (d) The SOT efficiency of the Te/MgO/Py as a function of the back-gate voltage.

limited by complex multilayer growth, low working temperatures, or slow ionic migration, the Te-based system exhibits distinct advantages. The Te-based heterostructure features a simple structure without extrinsic doping and a purely electronic nature. The back-gate voltage modulates carrier density by tuning the Fermi level position in the bandgap, thereby modifying the magnitude of the Berry curvature dipole in the valence band of Te.[28] This enables reliable room-temperature operation with fast dynamics. Moreover, due to the unique chiral crystal structure of Te, further optimization of the Te/ferromagnet interface can not only improve the tunability of SOT efficiency,[49] but also potentially generate unconventional spin polarization components.[31] This positions Te as a promising candidate for electrically tunable spintronic devices.

4. Conclusions. In summary, the effective gate tuning of the chiral anomaly-induced NMR was demonstrated in high-quality 2D single-crystalline Te flakes. The NMR magnitude peaked at $V_G = -7$ V, concurrent with the most pronounced weak localization effect, suggesting a common origin related to the Berry curvature. Furthermore, in Te/Py and Te/MgO/Py magnetic heterostructures, the SOT efficiencies were determined to be 0.12 and 0.089, respectively, comparable to those of conventional heavy metals. To suppress Fermi-level pinning at the interface between semiconductor and metal by inserting an ultrathin MgO layer, a gate-tunable SOT efficiency of 15% was subsequently realized in the Te-based heterostructure. Our findings establish 2D Te-based heterostructures as a promising material platform for high-performance, gate-tunable spintronic devices.

Acknowledgements. This work was supported by the National Natural Science Foundation of China (Grant Nos. 52501238, 52271237, 52130103, 12474106, 51971026, 12574124, and 52401225), the Joint Funds of the National Natural Science Foundation of China (Grant No. U21A20432), the open research fund of Songshan Lake Materials Laboratory (Grant No. 2022SLABFN07), and the Guangdong Provincial Quantum Science Strategic Initiative (Grant No. GDZX2501006).

References

[1] Behin-Aein B, Datta D, Salahuddin S, and Datta S 2010 *Nat. Nanotechnol.* **5** 266
[2] Wang X, Wan C, Kong W, Zhang X, Xing Y, Fang C, Tao B, Yang W, Huang L, Wu H, Irfan M, and Han X 2018 *Adv. Mater.* **30** 1801318
[3] Fukami S, Anekawa T, Zhang C, and Ohno H 2016 *Nat. Nanotechnol.* **11** 621
[4] Yan Z, Li Z, Zhu L, Lin X, and Zhu L 2025 *Chin. Phys. Lett.* **42** 090701
[5] Miron I M, Garello K, Gaudin G, Zermatten P J, Costache M V, Auffret S, Bandiera S, Rodmacq B, Schuhl A, and Gambardella P 2011 *Nature* **476** 189
[6] Liu L, Pai C F, Li Y, Tseng H W, Ralph D C, and Buhrman R A 2012 *Science* **336** 555
[7] Liu L, Moriyama T, Ralph D C, and Buhrman R A 2011 *Phys. Rev. Lett.* **106** 036601
[8] Pai C F, Liu L, Li Y, Tseng H W, Ralph D C, and Buhrman R A 2012 *Appl. Phys. Lett.* **101** 122404
[9] Yu G, Upadhyaya P, Fan Y, Alzate J G, Jiang W, Wong K L, Takei S, Bender S A, Chang L T, Jiang Y, Lang M, Tang J, Wang Y, Tserkovnyak Y, Amiri P K, and Wang K L 2014 *Nat. Nanotechnol.* **9** 548
[10] Fan Y, Upadhyaya P, Kou X, Lang M, Takei S, Wang Z, Tang J, He L, Chang L T, Montazeri M, Yu G, Jiang W, Nie T, Schwartz R N, Tserkovnyak Y, and Wang K L 2014 *Nat. Mater.* **13** 699
[11] Han J, Richardella A, Siddiqui S A, Finley J, Samarth N, and Liu L 2017 *Phys. Rev. Lett.* **119** 077702
[12] Hu S, Shao D F, Yang H, Pan C, Fu Z, Tang M, Yang Y, Fan W, Zhou S, Tsymbal E Y, and Qiu X 2022 *Nat. Commun.* **13** 4447
[13] Yoon J Y, Takeuchi Y, Takechi R, Han J, Uchimura T, Yamane Y, Kanai S, Ieda J, Ohno H, and Fukami S 2025 *Nat. Commun.* **16** 1171
[14] Shao Q, Yu G, Lan Y W, Shi Y, Li M Y, Zheng C, Zhu X, Li L J, Amiri P K, and Wang K L 2016 *Nano Lett.* **16** 7514
[15] Xie Q, Lin W, Yang B, Shu X, Chen S, Liu L, Yu X, Breese M B H, Zhou T, Yang M, Zhang Z, Wang S, Yang H, Chai J, Han X, and Chen J 2019 *Adv. Mater.* **31** 1900776
[16] MacNeill D, Stiehl G M, Guimaraes M H D, Buhrman R A, Park J, and Ralph D C 2017 *Nat. Phys.* **13** 300
[17] Wang F, Shi G, Kim K W, Park H J, Jang J G, Tan H R, Lin M, Liu Y, Kim T, Yang D, Zhao S, Lee K, Yang S, Soumyanarayanan A, Lee K J, and Yang H 2024 *Nat. Mater.* **23** 768
[18] Zhang Y, Xu H, Jia K, Lan G, Huang Z, He B, He C, Shao Q, Wang Y, Zhao M, Ma T, Dong J, Guo C, Cheng C, Feng J, Wan C, Wei H, Shi Y, Zhang G, Han X, and Yu G 2023 *Sci. Adv.* **9** eadg9819
[19] Liu Y, Shi G, Kumar D, Kim T, Shi S, Yang D, Zhang J, Zhang C, Wang F, Yang S, Pu Y, Yu P, Cai K, and Yang H 2023 *Nat. Electron.* **6** 732
[20] Xu H, Wei J, Zhou H, Feng J, Xu T, Du H, He C, Huang Y, Zhang J, Liu Y, Wu H, Guo C, Wang X, Guang Y, Wei H, Peng Y, Jiang W, Yu G, and Han X 2020 *Adv. Mater.* **32** 2000513

[21] Wang X, Tang J, Xia X, He C, Zhang J, Liu Y, Wan C, Fang C, Guo C, Yang W, Guang Y, Zhang X, Xu H, Wei J, Liao M, Lu X, Feng J, Li X, Peng Y, Wei H, Yang R, Shi D, Zhang X, Han Z, Zhang Z, Zhang G, Yu G, and Han X 2019 *Sci. Adv.* **5** eaaw8904

[22] Zhang Q, Xu H, Xu Z, He C, Li X, Lan G, Zhang J, Shi Y, Zhang Q, Yang C Y, Chen J, Gao Y, Hu C, Li J, Zhao Y, Huo Y, Ge J, Zhang Y, Chang H K, Huang C Y, Shen S, Zhang Y, Wei H, Yu G, and Wang S 2025 *Adv. Funct. Mater.* **35** 2414742

[23] Ostwal V, Shen T, and Appenzeller J 2020 *Adv. Mater.* **32** 1906021

[24] Reed E J 2017 *Nature* **552** 40

[25] Wang Y, Qiu G, Wang R, Huang S, Wang Q, Liu Y, Du Y, Goddard W A, Kim M J, Xu X, Ye P D, and Wu W 2018 *Nat. Electron.* **1** 228

[26] Ren X, Wang Y, Xie Z, Xue F, Leighton C, and Frisbie C D 2019 *Nano Lett.* **19** 4738

[27] Zhao C, Tan C, Lien D H, Song X, Amani M, Hettick M, Nyein H Y Y, Yuan Z, Li L, Scott M C, and Javey A 2020 *Nat. Nanotechnol.* **15** 53

[28] Cheng B, Li L, Zhang N, Zhang L, Li X, Lin Z, Li H, Wang Z, and Zeng C 2022 *Phys. Rev. Appl.* **17** 054044

[29] Lu J, He Y, Ma C, Ye Q, Yi H, Zheng Z, Yao J, and Yang G 2023 *Adv. Mater.* **35** 2211562

[30] Hirayama M, Okugawa R, Ishibashi S, Murakami S, and Miyake T 2015 *Phys. Rev. Lett.* **114** 206401

[31] Gupta R and Droghetti A 2024 *Phys. Rev. B* **109** 155141

[32] Wang M, Guo Q, Xu X, Zhang Z, Ren Z, Zhu L, Meng K, Chen J, Wu Y, Miao J, and Jiang Y 2020 *Adv. Electron. Mater.* **6** 2000229

[33] Vaz D C, Lin C C, Plombon J J, Choi W Y, Groen I, Arango I C, Chuvilin A, Hueso L E, Nikonov D E, Li H, Debashis P, Clendenning S B, Gosavi T A, Huang Y L, Prasad B, Ramesh R, Vecchiola A, Bibes M, Bouzehouane K, Fusil S, Garcia V, Young I A, and Casanova F 2024 *Nat. Commun.* **15** 1902

[34] Mishra R, Mahfouzi F, Kumar D, Cai K, Chen M, Qiu X, Kioussis N, and Yang H 2019 *Nat. Commun.* **10** 248

[35] Lee S, An S, Baek E, Kim D, Cho J, and You C Y 2025 *Sci. Adv.* **11** eadr0457

[36] Fan Y, Kou X, Upadhyaya P, Shao Q, Pan L, Lang M, Che X, Tang J, Montazeri M, Murata K, Chang L T, Akyol M, Yu G, Nie T, Wong K L, Liu J, Wang Y, Tserkovnyak Y, and Wang K L 2016 *Nat. Nanotechnol.* **11** 352

[37] Lv W, Jia Z, Wang B, Lu Y, Luo X, Zhang B, Zeng Z, and Liu Z 2018 *ACS Appl. Mater. Interfaces* **10** 2843

[38] Mihalceanu L, Keller S, Greser J, Karfaridis D, Simeonidis K, Vourlias G, Kehagias T, Conca A, Hillebrands B, and Papaioannou E T 2017 *Appl. Phys. Lett.* **110** 252406

[39] Li S, Zhao X, Liu W, Zhao X, and Zhang Z 2019 *Appl. Phys. Lett.* **114** 212404

[40] Ong N P and Liang S 2021 *Nat. Rev. Phys.* **3** 394

[41] Chen J, Zhang T, Wang J, Xu L, Lin Z, Liu J, Wang C, Zhang N, Lau S P, Zhang W, Chhowalla M, and Chai Y 2022 *Sci. Adv.* **8** eabn3837

[42] Niu C, Qiu G, Wang Y, Zhang Z, Si M, Wu W, and Ye P D 2020 *Phys. Rev. B* **101** 205414

[43] Kittel C 1947 *Phys. Rev.* **71** 270

[44] Garello K, Miron I M, Avci C O, Freimuth F, Mokrousov Y, Blugel S, Auffret S, Boulle O, Gaudin G, and Gambardella P 2013 *Nat. Nanotechnol.* **8** 587

[45] Pai C F, Ou Y, Vilela Leao L H, Ralph D C, and Buhrman R A 2015 *Phys. Rev. B* **92** 064426

[46] Wang Y, Ramaswamy R, and Yang H 2018 *J. Phys. Appl. Phys.* **51** 273002

[47] Maruggi G P, Ferreira J, Baggio-Saitovitch E, Enderlein C, and Silva Neto M B 2023 *Phys. Rev. Mater.* **7** 014204

[48] Hua Z, Niu C, Joy S, Tan P, Shi G, Liu H, Guo J, Graf D, Ye P, Lewandowski C, and Xiong P 2025 arXiv:2507.14292 [cond-mat.mtrl-sci]

[49] Wang Y and Chhowalla M 2022 *Nat. Rev. Phys.* **4** 101

[50] Lieten R R, Degroote S, Kuijk M, and Borghs G 2008 *Appl. Phys. Lett.* **92** 022106

[51] Li W, Gong X, Yu Z, Ma L, Sun W, Gao S, Koroglu C, Wang W, Liu L, Li T, Ning H, Fan D, Xu Y, Tu X, Xu T, Sun L, Wang W, Lu J, Ni Z, Li J, Duan X, Wang P, Nie Y, Qiu H, Shi Y, Pop E, Wang J, and Wang X 2023 *Nature* **613** 274

[52] Fang H, Tosun M, Seol G, Chang T C, Takei K, Guo J, and Javey A 2013 *Nano Lett.* **13** 1991